SEMARAK ILMU PUBLISHING

Journal of Advanced Research in Applied Mechanics

Journal homepage:
https://semarakilmu.com.my/journals/index.php/appl_mech/index
ISSN: 2289-7895

Large Eddy Simulation of Low Reynolds Number Flow around a NACA0015 Airfoil with Modified Trailing Edges

Mohamed Ibren Hassan[1], Amelda Dianne Andan[1,*], Waqar Asrar[1], Mohd Azan Mohammed Sapardi[1]

[1] Department of Mechanical Engineering, Faculty of Engineering, International Islamic University Malaysia, 53100, Kuala Lumpur, Malaysia

ARTICLE INFO

Article history:
Received 9 August 2023
Received in revised form 11 October 2023
Accepted 27 October 2023
Available online 5 January 2024

Keywords:
Large Eddy Simulation; NACA0015 Airfoil; Serration; Low-Reynolds Number

ABSTRACT

The flow field of a low Reynolds number regime is three-dimensional and exceedingly complicated due to numerous forms of vortical phenomena, which has triggered the interest of many researchers. This study aims to investigate the influence of various trailing edge configurations on the aerodynamic characteristics and flow structure of airfoils. Specifically, five different configurations, namely baseline, serration, comb, and comb-serration are analyzed in detail. The study seeks to identify the configuration that provides optimal aerodynamic performance, which can then inform the design of more efficient airfoils for a range of applications, including unmanned aerial vehicle (UAV), wind energy, and automotive design. A Large-eddy simulation numerical model was developed to effectively evaluate unsteady pressure fluctuations and turbulence parameters at the source. The pressure coefficient and skin friction coefficient figures reveal that modifications result in an early negative pressure zone and uneven flow along the airfoil surfaces. This study presents numerical findings on the NACA0015 airfoil at a zero angle of attack. The pressure coefficient distribution along the airfoil surface exhibits a symmetrical pattern, with the highest pressure observed at the leading edge due to flow deceleration. Analysis of the skin friction coefficient confirms the absence of separation zones on the airfoil surface, except for the tip of the trailing edge. The velocity profile demonstrates a consistent and smooth flow, indicating stable and symmetrical conditions across the airfoil. Moreover, the velocity profiles of the baseline airfoil at zero angle of attack do not indicate any signs of flow separation. Notably, the serrated, combed and comb-serrated trailing edge configurations each yield distinctive effects on fluid flow. The serrated trailing edge promotes increased fluid velocity and pressure drop, while the combed configuration induces separation at the root. Meanwhile, the comb-serrated design sustains a continuous fluid flow over the airfoil surface. Overall, these results contribute to a comprehensive understanding of the aerodynamic behavior and flow characteristics influenced by various trailing edge configurations.

* *Corresponding author.*
E-mail address: ameldadianne@iium.edu.my

https://doi.org/10.37934/aram.112.1.5779

1. Introduction

The complexity of the low Reynolds number regime triggered the interest of many researchers. The issues related to the flow field within low Reynolds numbers are important in the design of sophisticated unmanned aerial vehicles and wind turbines that have industrial applications. Furthermore, computer simulation has emerged as a cost-effective method for comprehending the underlying physics of flow structures over airfoils. By harnessing the power of computer simulations, a more precise visualization of flow topology becomes attainable, thereby facilitating the identification of optimal flow conditions with greater ease.

This flow regime is three-dimensional and overly complex due to various forms of vortical phenomena. The flow structures around an airfoil are entirely different for a wide range of Reynolds numbers. Flow separation and formation of laminar separation bubbles (LSB) are among the key features found in this flow regime [1]. The flow separates due to a strong adverse pressure gradient [2,3]. Moreover, stronger adverse pressure gradients and weaker fluid momentum would keep the flow separated, hence forming a considerable wake region downstream of the trailing edge [4]. Likewise, the separated flow field may interfere with the laminar boundary layer (LBL) and begin to form unstable shear layers known as hydrodynamic instabilities. These shear layers disintegrate inconsistently into a chaotic flow [5] due to the changes in the fluid pressure and velocity [6]. On the other hand, the separated flow might go through a transition to turbulence [3,5] and thus the turbulent boundary layer (TBL) is formed in the wake of a vortical structure known as reverse flow [3]. This trend is because of an increase in the fluid momentum after the transition. Consequently, the accelerated shear layers reattach to the airfoil surfaces to develop a region of low velocity and low pressure known as a laminar separation bubble [3,5,7]. Besides that, the laminar separation bubble might separate or reattach again after the trailing edge [4].

The laminar separation bubble is often categorized into long and short bubbles [8]. This classification was based on the length scales of displacement thickness at the separation point and the chord length. Long bubbles affect pressure fluctuations, whereas short bubbles can alter the potential flow over the airfoil surface [3]. Additionally, the size of the bubble formed depends on the Reynolds number of the flow, the bubble might form, burst, or vanish due to a slight change in the Reynolds number [9,10]. For instance, short bubbles at times burst to form a huge bubble that either reattaches with the surface or flows towards the wake without reattachment. The bursting of the bubbles controls the stalling of an airfoil [3]. The features of the bubbles do not depend on Reynolds number only but also on the angle of attack (AoA) [11]. At smaller angles of attack (below stall angle), the bubbles determine the transition behavior of the flow. The bubbles are formed on both sides of the airfoil for small angles of attack. When the angle of attack is increased, the size and the length of the laminar separation bubble decrease gradually. Concurrently, the bubbles rapidly shift towards the leading edge on the airfoil suction side [12], whereas the boundary layer moves closer to the trailing edge on the pressure side [13]. Moreover, airfoil geometry and turbulence intensity affect the wake features, for example, the vortex size, rotational direction, and shedding frequency [14,15] as well as the wind turbine performance [16]. Some studies have demonstrated the dependence of aerodynamic performance [4] and radiated noise [17] over 2D airfoils towards flow conditions at relatively low Reynolds numbers. A slight change in the airfoil profile would alter the lift coefficient, separation features, and stalling behavior [18]. Similarly, separation location and stalling characteristics affect aircraft structure and aerodynamic performance [19]. This has sparked interest among researchers in developing effective control tools capable of mitigating noise without affecting aerodynamic performance. Consequently, a thorough analysis and understanding of the near-field features are necessary.

In recent years, the application of modified trailing edges such as serrated, has been demonstrated experimentally [3,20-24] and numerically [25,26] that it can minimize noise generated at the trailing edge. However, in most cases, these serrations are made into a thin flat plate and inserted into the main body of the airfoil [27]. Theoretically, the geometry of the serration destructs the coherent structure between the acoustic waves, thus altering the acoustic radiation along the span. After that, noise reduction is achieved due to the interference of acoustics at the source [28,29]. On the contrary, an experimental work examining the wall pressure power spectral density and the coherent structure along the serration edges shows that the flow field is almost identical [30]. Nevertheless, they have also observed vortices along the serration edges thus affecting the momentum and turbulence energy distribution [30]. The vortices near the serration trailing edges will affect the acoustic radiation, which will reduce the trailing edge noise [31]. Based on other studies [32-34], serration affects the flow-field structure, by reducing the amplitude of the unsteady pressure fluctuations along the span hence at times it is referred to as the source cut-off effect. Following one of the studies [33], the unsteady pressure fluctuations at the source have a direct influence on the noise generated. Therefore, reducing the pressure fluctuations at the source will affect the overall noise generated. Yet another study revealed that the serration model produces lift and drag coefficient profiles similar to the baseline within specific angles of attack [35].

Another exceptional technique that is incorporated with serration design is poro-serrated. This approach offers further noise reduction [36]. Moreover, metal foams and porous coatings covering a circular cylinder have shown notable noise reduction due to the stability of the vortical and turbulence structure near the wake [37,38]. The most frequently used parameters to describe porous materials are porosity, airflow resistivity, and tortuosity [39,40]. Porosity can be defined as the measure of the void space in a material whereas resistivity indicates the ability of a material to oppose the flow through its void spaces [1]. The porous material should be permeable to the acoustically normal component velocity at the source and impermeable to the average flow velocity. This reduces the unwanted flow leakage and thus maintains the aerodynamic performance [39]. Over and above that, the porosity should progressively increase downstream of the porous material. However, this cannot be achieved with cutting insertions due to the introduction of surface discontinuity [39].

Some recent studies have confirmed that a porous trailing edge has the potential to reduce trailing-edge noise due to the breakdown of spanwise pressure fluctuations [41-43] and a decrease in streamwise convection velocity [43]. The underlying mechanisms that show the capability of porous treatment in reducing noise generated are linked to the stabilization of turbulence structures [41,44,45], attenuation of vortex shedding [41,46], controlling of flow-induced instabilities such as pressure distributions and fluctuations [41,45] as well as minimizing the acoustical dipole strength near the wake [31]. For instance, some of the concepts that can be applied to reduce vortex shedding are the utilization of smaller pore size with a sub-millimeter diameter as well as correct placement of the porous region on the airfoil's surface [46], which will reduce pressure fluctuation and peak swirl velocity; consequently, reducing the generated noise [47]. Moreover, the artificial thickening of the turbulent boundary layer on both sides of the airfoil is believed to be the main cause of surface roughness noise [48].

Reynolds-averaged Navier–Stokes (RANS) is incapable of computing the unsteady solution at the source accurately due to the enormous range of scales involved [49]. Therefore, in this paper, the fluid-flow analysis is performed using incompressible large eddy simulation (LES) that enables well-resolved and detailed information of the unsteady flow to be generated around the wing [50]. The main concept of LES is to compute the filtered Navier-Stokes equations for the large-scale eddies and analyze the effect of small-scale eddies using sub-grid scale (SGS) [51]. This approach is a promising

model that effectively evaluates unsteady pressure fluctuations and turbulence parameters at the source [49]. LES is suitable and applicable for examining complex fluid-flow structures [51].

The current study describes the development and the effects of various passive control methods used for noise reduction, on the fluid flow field around a NACA 0015 airfoil placed at zero angle of attack. The flow condition is at a chord-based Reynolds number of 1.6 x 10^5. This study has relevance to various applications such as unmanned air vehicles (UAV), and wind turbine blades, all of which function at relatively low Reynolds numbers. To further assess the influence of different serration designs on the flow parameters, combed and comb-sawtooth trailing-edge were included in the CFD analysis. In this current work, streamwise velocity components, velocity profile along the airfoil's top surface, and vortical structures are investigated and presented. The mean flow variables and the instantaneous quantities are computed and compared with other studies.

2. Methodology

2.1 Numerical Scheme

Large-eddy simulation is a numerical technique that filters the original Navier–Stokes equations to accurately solve complex unsteady transient simulation with less computational time and space. However, the smallest (sub-grid) perturbations less than the integral length scale are resolved by a model known as the turbulence closure problem [52]. The filtered version can be performed explicitly or implicitly or even combining both [50].

Filtered Navier–Stokes equation and continuity equations for incompressible flow can be written as [53]:

$$\frac{\partial}{\partial t}\left(\rho\underline{u}_i\right) + \frac{\partial}{\partial x_j}\left(\rho\underline{u}_i\underline{u}_j\right) = \frac{\partial}{\partial x_j}\left(\sigma_{ij}\right) - \frac{\partial \underline{p}}{\partial x_i} - \frac{\partial \tau_{ij}}{\partial x_j} \tag{1}$$

$$\frac{\partial \rho}{\partial t} + \frac{\partial}{\partial x_i}\left(\rho\underline{u}_i\right) = 0 \tag{2}$$

where σ_{ij} is the stress tensor, it is interpreted as follows

$$\sigma_{ij} = \left[\mu\left(\frac{\partial \underline{u}_i}{\partial x_j} + \frac{\partial \underline{u}_j}{\partial x_i}\right)\right] - \frac{2}{3}\mu\frac{\partial \underline{u}_i}{\partial x_i}\delta_{ij} \tag{3}$$

and τ_{ij} is the subgrid-scale (SGS) stress tensor illustrated as

$$\tau_{ij} = \rho\underline{u_i u_j} - \rho\underline{u}_i\underline{u}_j \tag{4}$$

Nonetheless, the subgrid-scale stress tensor is unknown and thus modeled based on isotropic assumptions as shown by Eq. (5)

$$\tau_{ij} - \frac{1}{3}\tau_{kk}\delta_{ij} = -2\nu_{sgs}\underline{S}_{ij} \tag{5}$$

where ν_{sgs} is the subgrid-scale kinematic viscosity and $\underline{S}_{ij}$ is the strain rate from the smallest resolved eddies. The rate of strain tensor is defined as

$$\underline{S}_{ij} = \frac{1}{2}\left(\frac{\partial \underline{u}_i}{\partial x_j} + \frac{\partial \underline{u}_j}{\partial x_i}\right) \tag{6}$$

In addition, the subgrid-scale kinematic viscosity is undetermined and thus becomes the variable to be evaluated. Based on the original Smagorinsky method [54], SGS viscosity is computed as follows

$$\nu_{sgs} = C_s \underline{\Delta}^2 \left|\underline{S}\right| \tag{7}$$

where C_s is the model constant, also referred to as the Smagorinsky coefficient. It describes the ratio of the cell size that gives the average eddy in a cell, it ranges from 0 to 1 because it is expected to be less than the cell size. The second term on the right side of Eq. (7) ($\underline{\Delta}$) is the subgrid filter width, which defines the mesh size. Lastly, $\left|\underline{S}\right|$ is the modulus of the strain rate tensor, which is equivalent to $\sqrt{2\underline{S}_{ij}\underline{S}_{ij}}$.

Following the computation of subgrid-scale kinematic viscosity, subgrid-scale stress tensor can now be presented as shown by Eq. (8)

$$\tau_{ij} - \frac{1}{3}\tau_{kk}\delta_{ij} = -2C_s \underline{\Delta}^2 \left|\underline{S}\right| \underline{S}_{ij} \tag{8}$$

However, the optimum C_s value varies for each part of the flow and must be reduced near solid walls to minimize the numerical dissipation introduced by the sub-grid scale model, this is particularly the case for wind turbine blades where the surface fluctuations are assumed to be the main acoustic sources. Therefore, the dynamic Smagorinsky method can be used [55].

In this model an extra filter level known as the test filter ($\tilde{\Delta}$) is used in combination with the sub-grid scale filter level, to estimate a value of $C_{s,new}$, which is a function of time and space [56]. Following Germano's [55] evaluation, the two filters were compared as follows.

$$\tilde{L}_{ij} = \underline{u_i u_j^{\check{}}} - \underline{\widetilde{u}_i}\,\underline{\widetilde{u}_i} \tag{9}$$

where $\tilde{L}_{ij}$ can be computed using resolved eddies in a cell as shown by Eq. (10)

$$\tilde{L}_{ij} = 2C_{s,new}\underline{\Delta} M_{ij} \tag{10}$$

where M_{ij} is defined as

$$M_{ij} = \left(\frac{\tilde{\Delta}}{\underline{\Delta}}\right)^2 \widetilde{\left|\underline{S}\right|}\,\widetilde{\underline{S}_{ij}} \tag{11}$$

Moreover, the new model constant ($C_{s,new}$) that provide stable solutions during the analysis is presented by Eq. (12)

$$C_{s,new}\underline{\Delta}^2 = \frac{L_{ij}M_{ij}}{M_{ij}M_{ij}} \tag{12}$$

2.2 Model Description

The present study focuses on the aerodynamic analysis of a NACA 0015 airfoil with a chord length of 0.15 m and a span length of 0.298 m, as depicted in Figure 1. The airfoil design was such that it

extended across the entire test section. The design of the trailing edge was intentionally kept rounded to alleviate the complexity in meshing for the computational model, and to address the limitations posed by sharp trailing edges in manufacturing. The fabrication of sharp trailing edges often presents difficulties, so a rounded shape was deemed a more feasible solution. Moreover, to capture the three-dimensional flow characteristics, a 3-D analysis was performed to improve the accuracy of the results, despite the higher computational time required compared to two-dimensional models. However, three-dimensional analyses provide relatively more accurate results. They are less susceptible to 3-D perturbations at high Reynolds numbers [57], which makes them well-suited for this study which is performed at relatively low Reynolds numbers.

In addition to the baseline NACA 0015 airfoil, the study also examines other trailing edge configurations, including serrated, comb, and comb-serrated, as displayed in Figure 2. The parameters employed for the serration, comb, and comb-serration configurations in this study are based on established references [28,52]. These configurations are a result of modifications made to the airfoil's trailing edge, located around 30% of the trailing edge. For instance, the serrated model involved the addition of sawtooth-like projections to the airfoil surface, with serration height, wavelength, and angle parameters of 38.55 mm, 8 mm, and 6 degrees, respectively. The comb modification consisted of parallel ridges with a comb height of 38.55mm and a comb spacing of 5mm. Additionally, the comb-serrated configuration was a combination of both serrated and comb configurations and was defined by the parameters of serration height (38.55 mm), serration wavelength (6.5 mm), comb height (38.55 mm), and comb spacing (1 mm). This examination aims to assess the impact of these modifications on the aerodynamic performance and flow structure, thereby expanding our understanding of how airfoil trailing edge modifications can impact aerodynamic behavior.

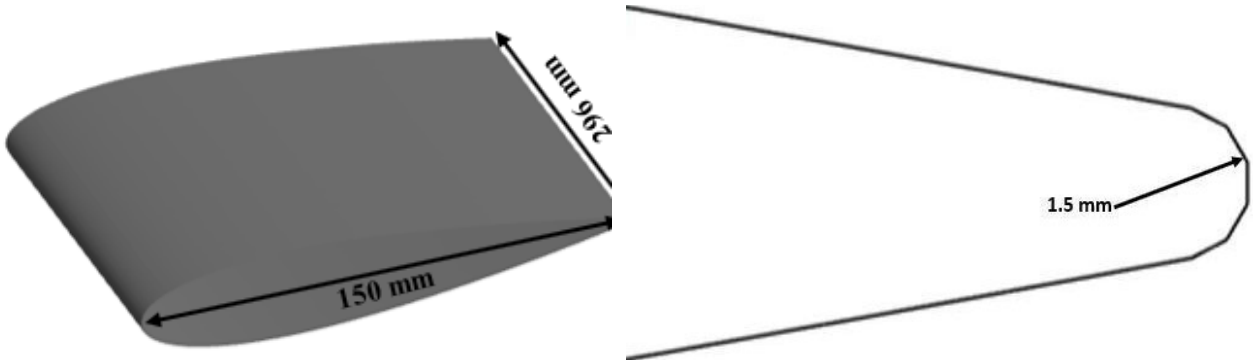

Fig. 1. Geometry of NACA0015 airfoil used in this study

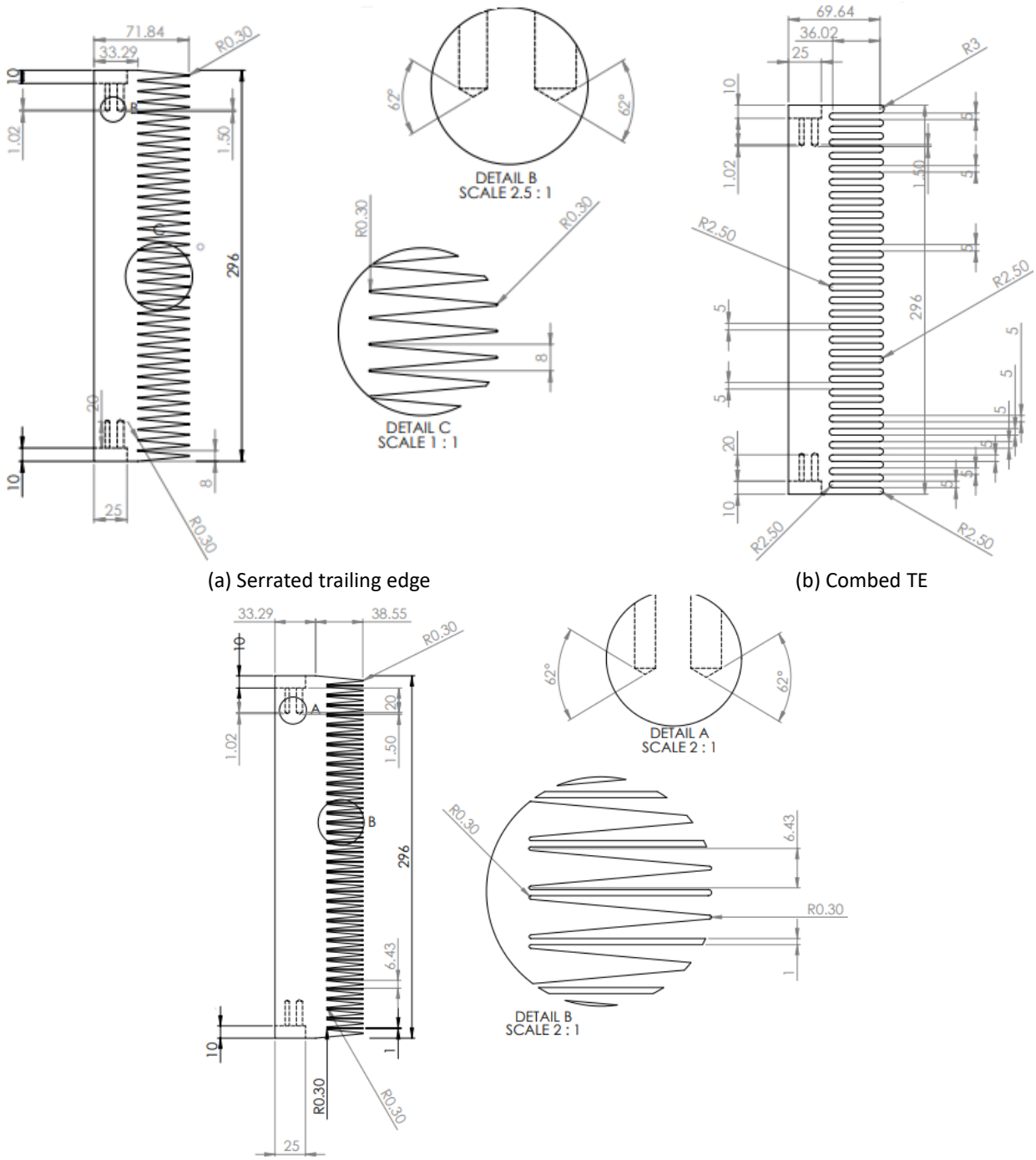

(a) Serrated trailing edge

(b) Combed TE

(c) Comb-serrated TE

Fig. 2. Geometry of all the trailing-edge sections used in this study

2.3 Computational Analysis

The computational domain (Figure 3) used to numerically investigate the flow field was about 15 airfoil chords upstream, above and below the airfoil surface. Additionally, it covers 30 airfoil chords downstream; this was considered to capture the wake region and ensure uniform freestream condition at the inlet [6]. The mesh is composed of 3 parts. The first shell is the partition for the finest mesh near the airfoil walls since it is the closest to the boundary layer region. The fine mesh assists in terms of the boundary layer resolution. The rest of the shells are subdivided next to each other, following the first shell. The division provides an easy way to have a finer and well-distributed mesh

around the area of most interest. An unstructured C-H grid topology was selected, as shown in Figure 4 (a)-(b). The y^+ value was computed and found to be approximately 0.9. This value defines the wall resolution in that the boundary layer effects are captured well, especially near the viscous sublayer.

Considering the main points of focus are the airfoil surfaces, the cell sizes are reduced to about 2 mm. A relatively finer grid at those locations enhances the accuracy of the computational outputs. Likewise, finer mesh allows the spectrum of high frequencies to be captured. Similarly, the computational mesh for a serrated, comb, or comb-serrated model typically employs an unstructured grid approach. The mesh refinement is done in areas close to the trailing edge, due to the complex geometry and boundaries of the physical domain. The mesh refinement allows the grid to accurately capture important geometric and flow features such as sharp edges, narrow gaps, or high gradients. For instance, in a serrated configuration, a sawtooth-like triangular shape is positioned between the serration surfaces to accurately represent the complex geometry of the trailing edge. This approach ensures a more precise representation and computational results.

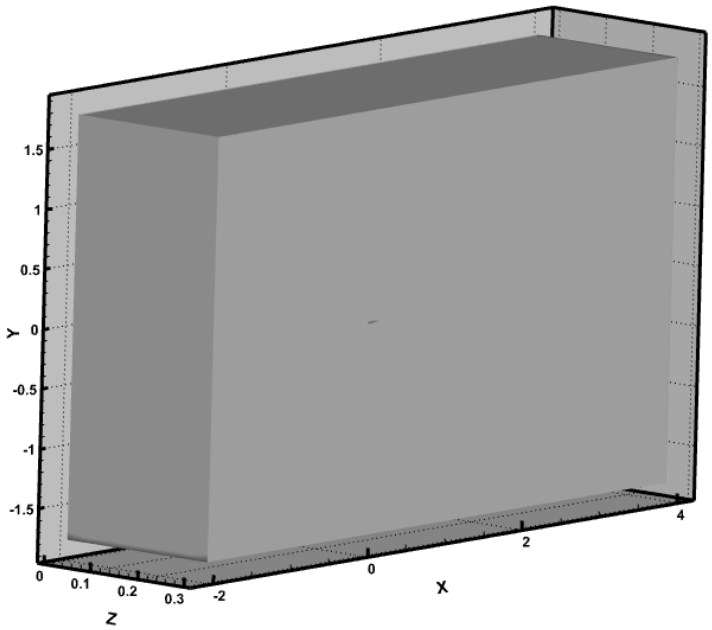

Fig. 3. Diagram of the domain used in the present work

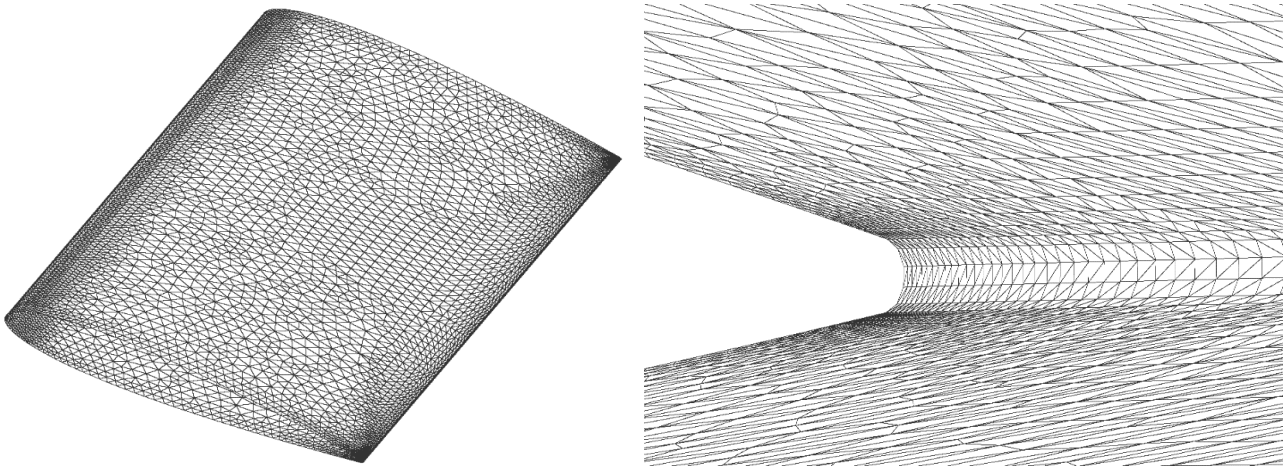

(a) Mesh around the wing surface (b) Close-Up view of TE part

Fig. 4. Close-up view of the mesh around the surface and at the trailing edge

A large-eddy simulation model was used to analyze the unsteady fluid flow within the computational domain. The sub-grid viscosity values were computed based on the dynamic Smagorinsky model (DSM), thus the Smagorinsky constant will be a local value. This approach enhances the accuracy of the results specifically near the wall compared to the original Smagorinsky model which uses a single value for all the cases.

The pressure-velocity integrating scheme used is Simplec, and the gradients were evaluated based on the Green-Gauss node-based technique. A second-order upwind discretization scheme was utilized to solve all the equations. Finally, a bounded second-order implicit scheme has been selected to set an appropriate time-dependent solution formulation.

A Fixed time-stepping scheme was used to evaluate the simulation. After examining a few time intervals, a dimensionless time of 160 based on free-stream velocity and airfoil chord was found sufficient for different cases. This has been reaffirmed by observing both instantaneous and averaged lift (Cl) and drag coefficients (Cd). The total time used for the simulation was initially estimated via the "hydraulic retention time" method. Nevertheless, the estimated flow time was doubled to have enough time for the flow to wash through the domain twice. Moreover, double precision was enabled so that the truncation error was reduced. This scheme has been verified with drag and lift coefficient plots.

3. Comparison and Validation of Numerical Method

3.1 Verification of Aerodynamic Coefficient

Several validations of the results have been conducted in the present study. Amongst useful resolution checks is to compare the mean lift coefficient of the present study with experimental study of similar parameters. Figure 5 shows the average lift coefficients of NACA 0015 measured using the present numerical model, compared to a published study [6] and experimental work [58,59]. The lift coefficient pattern is quite satisfactory at all angles of attack. The model sufficiently predicts an increase in the mean lift coefficient value as the angle of attack increases. However, the SST $\gamma - Re\theta$ model based on two-dimensional analysis displayed a slight over-prediction of the mean lift coefficient value above an angle of attack of 20. Moreover, the same pattern is still observed as the angle of attack increases. Generally, a good agreement between the present work and the experimental results is observed for all angles of attack. It should be noted that the experimental data [59] and the present study were obtained at a relatively lower Reynolds number of about Re = 1.6×10^5, whereas other studies, including the two-dimensional analysis, reported data at slightly higher Reynolds numbers of Re = 1.7×10^5.

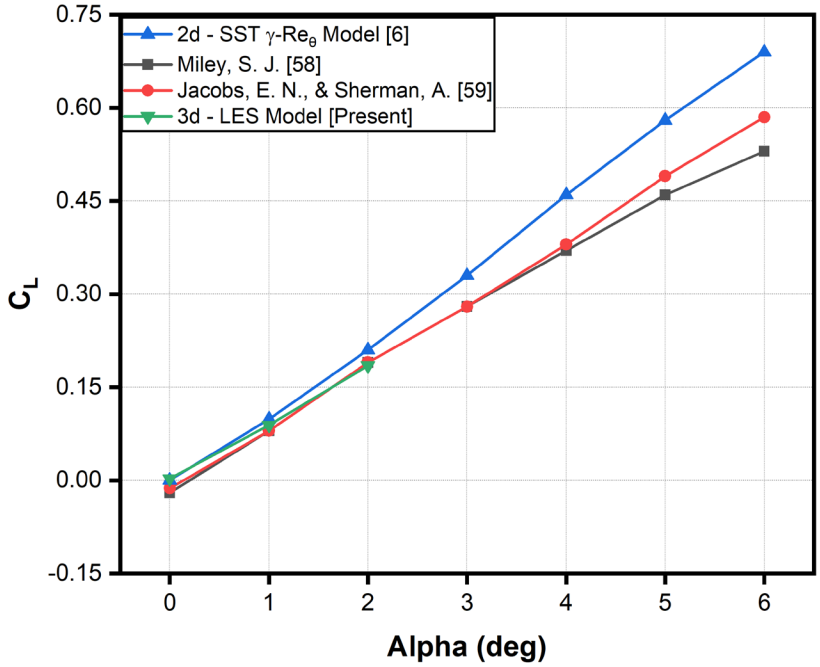

Fig. 5. Validation of the predicted values with the experimental data

4. Three-Dimensional Computational Analysis

4.1 Baseline Flow Field

Figure 6 (a)-(b) exhibits the variation of pressure and skin friction coefficient distribution over the surface of the NACA0015 airfoil at a zero angle of attack and a Reynolds number of 1.6 x 10^5. The pressure coefficient graph showed a symmetrical pressure distribution along the airfoil's surface. The maximum pressure is detected along the leading edge as anticipated due to the flow slowing down in this region. Moreover, a smooth pressure gradient is evident along the surface, and greater changes towards the leading edge and a progressive drop in the pressure towards the trailing edge. On the other hand, the skin friction coefficient reconfirmed the absence of a separation zone over the airfoil's surface, except for the tip part of the trailing edge. This is shown by the negative values of the skin friction coefficient. Generally, the pattern is seen decreasing from the leading towards the trailing edge, with the highest value at the leading edge. The figure indicated that the surface suffers comparatively modest low skin friction drag force at zero angle of attack.

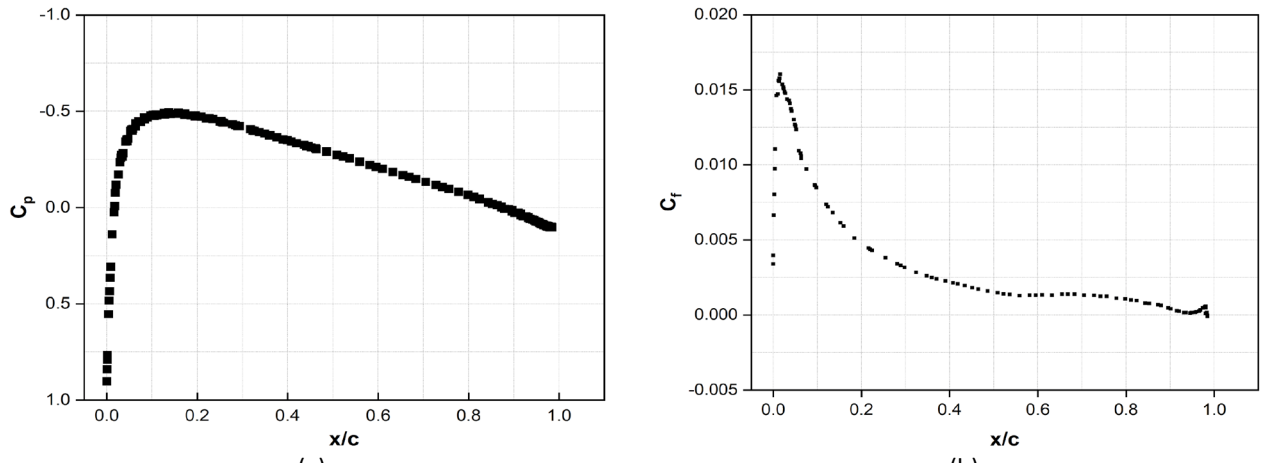

(a) (b)

Fig. 6. Pressure and skin friction coefficient of the baseline airfoil at α = 0^0

The mean x-velocity contour in Figure 7 (a)-(d) demonstrates the symmetrical flow pattern found at a zero angle of attack. This trend is underlined by the uniform velocity magnitude present on the airfoil's top and lower surfaces. As one advances from the leading edge, the velocity progressively increases until reaching a maximum near the mid-chord. The velocity then declines until reaching roughly zero at the trailing edge, as seen by the detailed picture (Figure 7). This phenomenon is aligned with the rules of fluid mechanics, which suggest that the velocity of fluid rises in regions with decreasing pressure. Additionally, due to the airfoil's blunt design, the flow is distinguished by its smoothness and absence of separation along the surface until after the tip of the trailing edge. The streamlines are also observed to be straight and parallel, resulting in a steady and uniform velocity distribution.

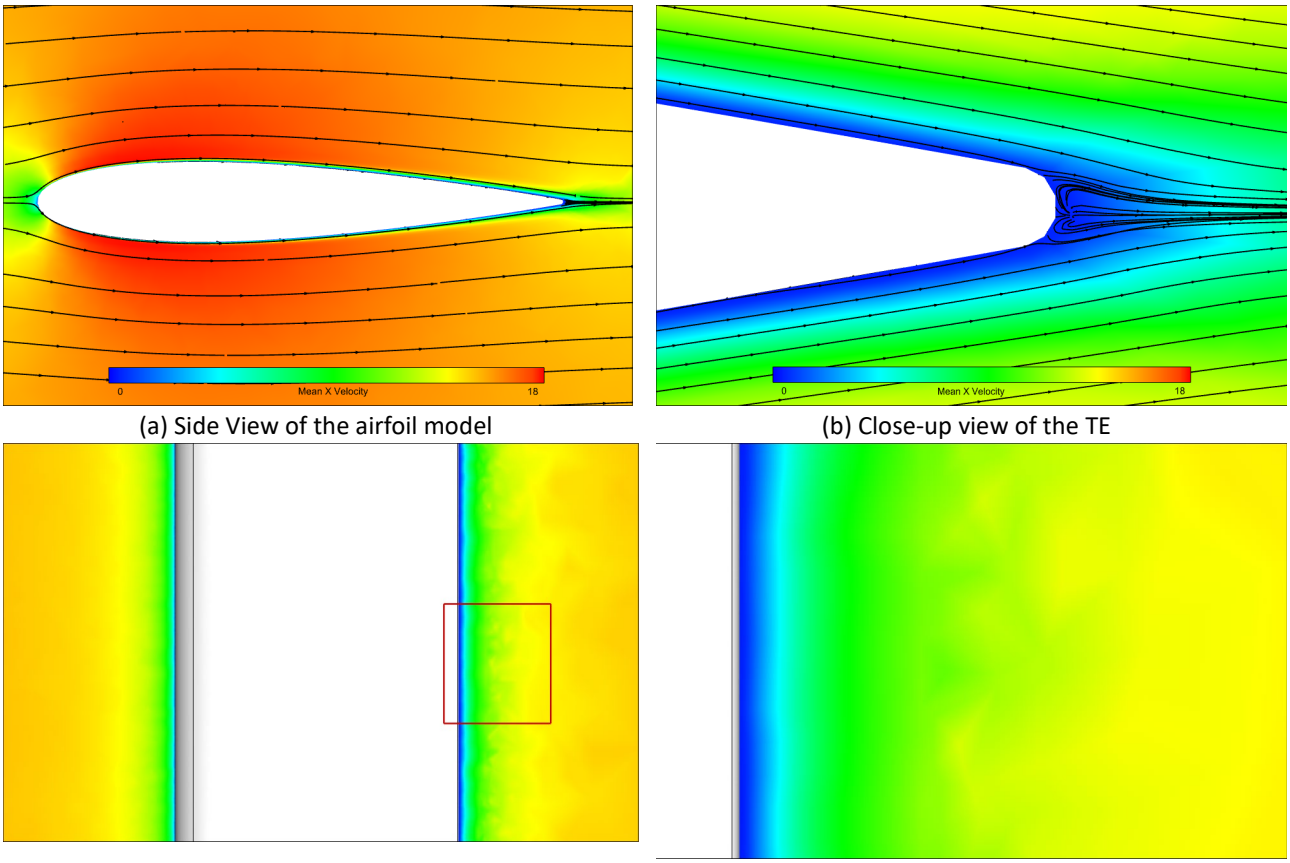

(a) Side View of the airfoil model (b) Close-up view of the TE

(c) Top view of the airfoil model (d) Close-up view of the TE

Fig. 7. X-velocity magnitude of the baseline airfoil at $\alpha = 0^0$

The velocity profile of an airfoil at a zero angle of attack plays a key role in defining the overall aerodynamic performance of the airfoil. The baseline model has a well-defined velocity profile at a zero angle of attack, which is represented in Figure 8. The velocity profile plot illustrates a smooth and consistent distribution of velocities throughout the airfoil's chord. This pattern can be due to the symmetrical and stable flow conditions occurring across the airfoil's surface at zero angle of attack. Furthermore, following the observation of the velocity profile gradient, it can be noted that the velocity magnitudes increase as one approaches away from the leading edge. Lastly, the velocity profiles of the baseline design at zero angle of attack do not display any signs of flow separation over the airfoil surface. The lack of a rapid change in the velocity gradient and a reversed flow region indicates the absence of flow separation. These imply a regular and well-behaved flow.

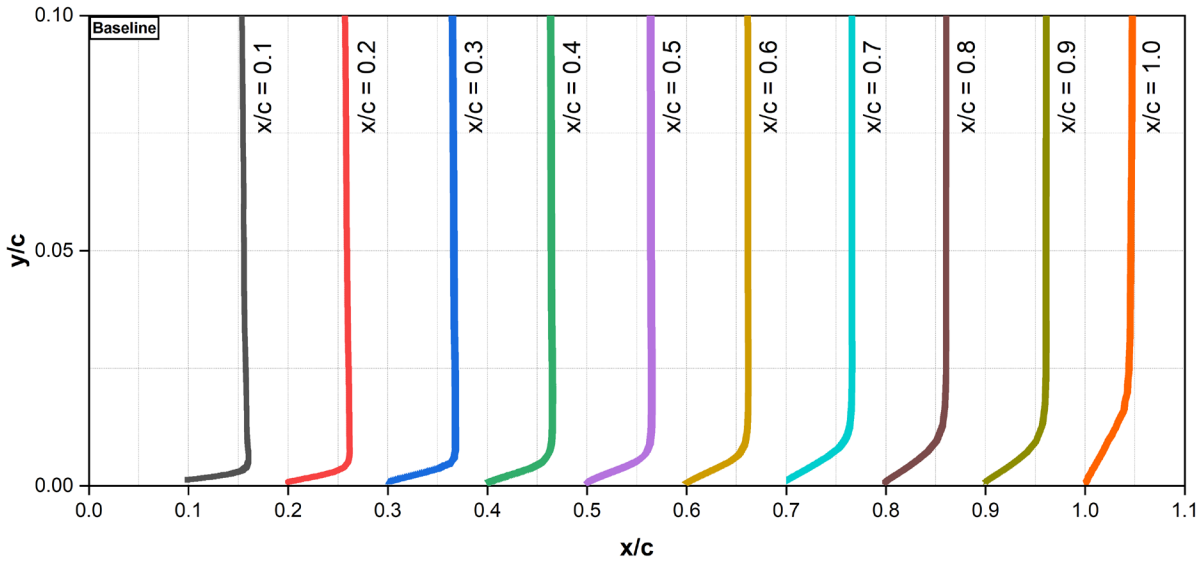

Fig. 8. Velocity Profile of the baseline airfoil at $\alpha = 0^0$

4.2 Modified Trailing-Edge Flow Field

The pressure coefficient graph, which is used to analyze the influence of serration, comb, and comb-serrated modifications on the trailing edge, is displayed in Figure 9 (a)-(c). This graph gives vital information on the distribution of pressure throughout the airfoil's surface and enables a full evaluation of the aerodynamic performance impact of these adjustments. It is shown that all modifications result in an early negative pressure zone near the trailing edge when compared to the baseline model, with the earliest detected in the serration and comb models and a later occurrence in the comb-serrated model. These adjustments are known to redistribute the flow over the airfoil's surface, resulting in changed flow structures. Despite this, identical pressure levels are seen at the leading edge, which results from the adjustments being positioned near the trailing edge rather than the leading edge. Like the baseline design, the pressure rises dramatically near the leading edge and progressively declines. The skin friction coefficient graph for the serration, comb, and comb-serrated trailing edge modifications at a zero angle of attack is provided in Figure 10 (a)-(c). The comparison between the baseline model and the modified trailing edges is visible in this graph. The serrated trailing edge reveals a separated flow, resulting in a tiny separation bubble at the trailing edge, as evidenced by a negative zone in the skin friction coefficient plot. On the other hand, the comb structure demonstrates a lower variability in skin friction compared to the baseline configuration. This trend can be due to the comb structure that alters the fluid flow towards the trailing edge, thereby decreasing turbulence and providing a more uniform flow. All the modified models, however, still display an uneven flow with greater skin friction values near the trailing edge. The pattern is due to the interaction between the flow and the redesigned trailing edges, generating turbulence and enhancing the fluid's momentum that is transmitted to the airfoil's surface.

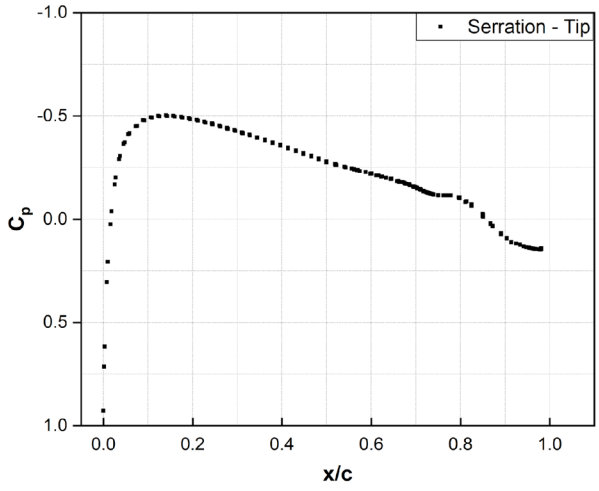

(a) Serrated TE

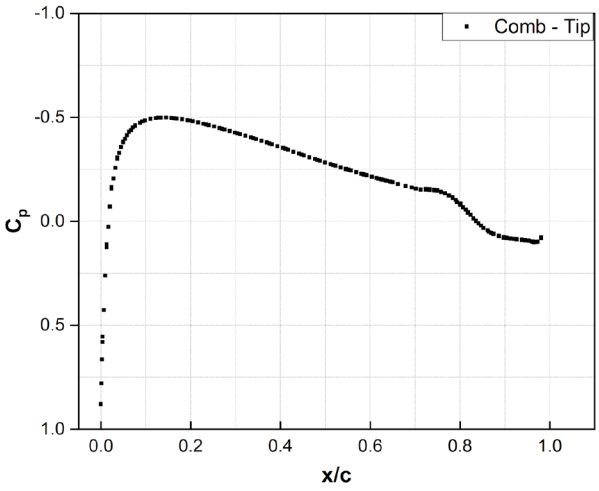

(b) Combed TE

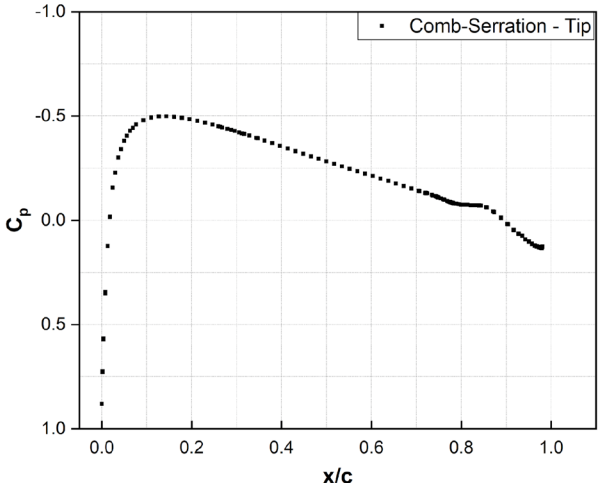

(c) Comb-Serrated TE

Fig. 9. Pressure coefficient of the modified models at $\alpha = 0^0$

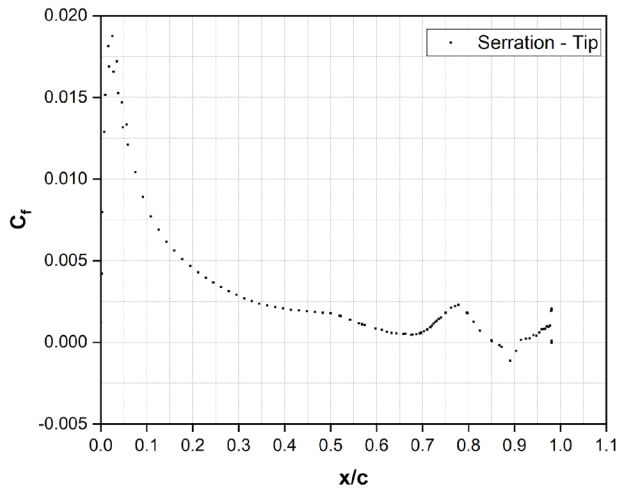

(a) Serrated TE

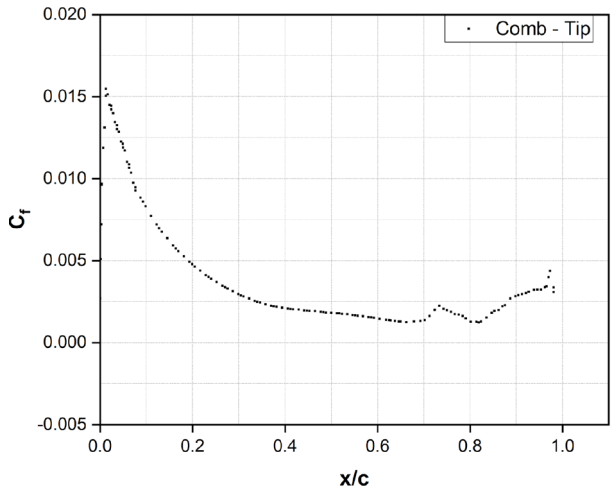

(b) Combed TE

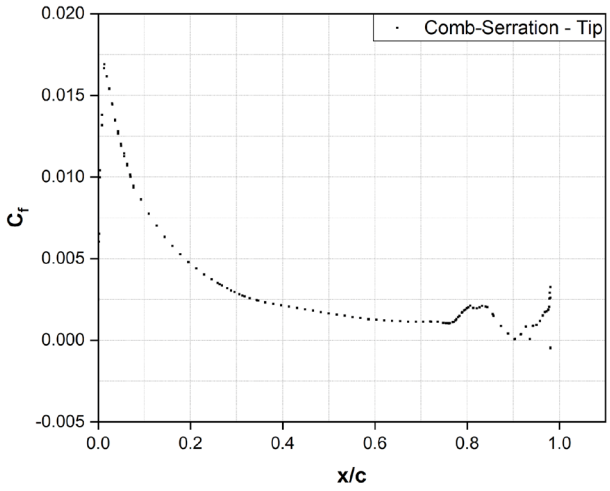

(c) Comb-Serrated TE

Fig. 10. Skin friction coefficient of the modified models at $\alpha = 0^0$

The x-velocity contours of serration, comb, and comb-serrated designs at a zero angle of attack are presented in Figure 11 (a)-(f), Figure 12 (a)-(f), and Figure 13 (a)-(f). This analysis gives additional insight into the influence of these adjustments on aerodynamic characteristics. At a zero angle of attack, it is noticed that the flow separates at the tip and root regions of the modified trailing edges, which is ascribed to the existence of surface structures that perturb the boundary layer and cause it to separate from the surface (Figure 11). On the other hand, the comb structure does not display any separation of the flow due to its perpendicular alignment with the surface, which helps maintain a smooth flow. The comb-serrated layout, however, is seen to efficiently retain a somewhat regular flow and demonstrate flow separation too, showing that the alteration effectively incorporates the effects of both the serrated and comb configurations. Additionally, a thorough analysis of Figure 12 indicates that the flow separates significantly along the roots of the serrated and comb models. In contrast, only a slight separation is noted for the comb-serrated design. This separation is a consequence of the bluntness present along the root of the trailing edge. Furthermore, Figure 13 gives a complete illustration of the flow patterns of the models, revealing that the comb slows down the flow more severely near the root of its trailing edge, followed by serration, and eventually, the comb-serrated arrangement.

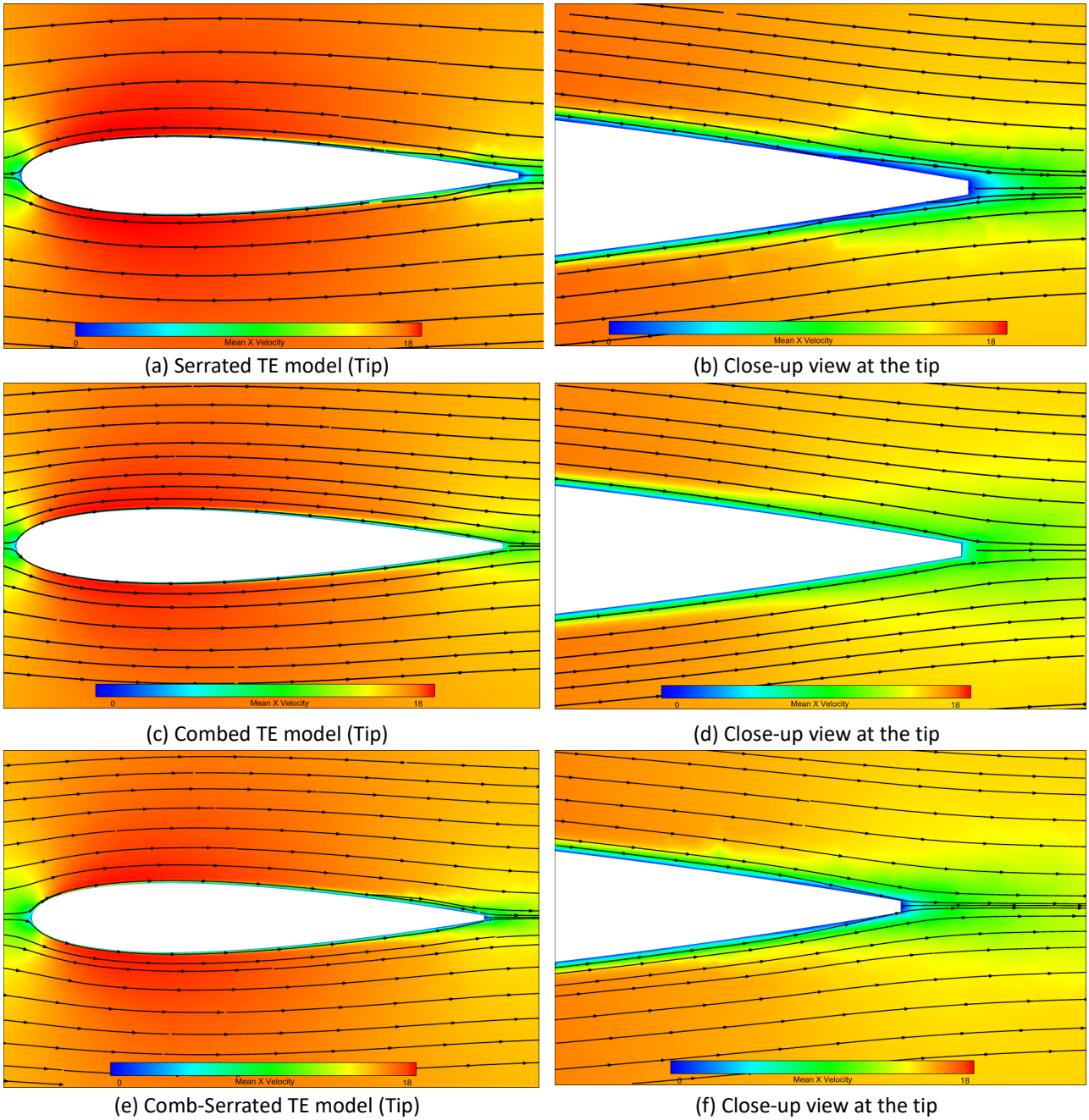

(a) Serrated TE model (Tip) (b) Close-up view at the tip

(c) Combed TE model (Tip) (d) Close-up view at the tip

(e) Comb-Serrated TE model (Tip) (f) Close-up view at the tip

Fig. 11. X-velocity contour at the tip of the modified models at $\alpha = 0^0$

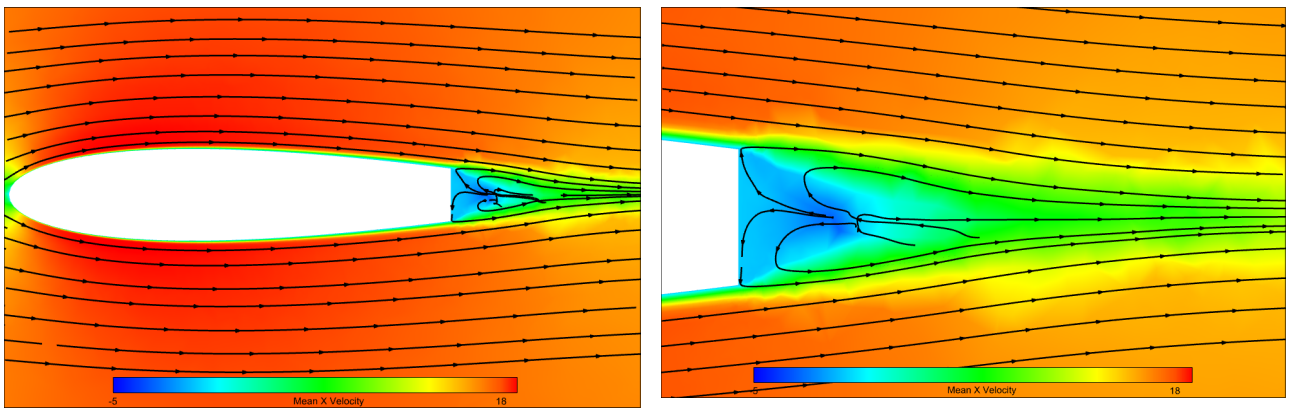

(a) Serrated TE model (Root) (b) Close-up view at the root

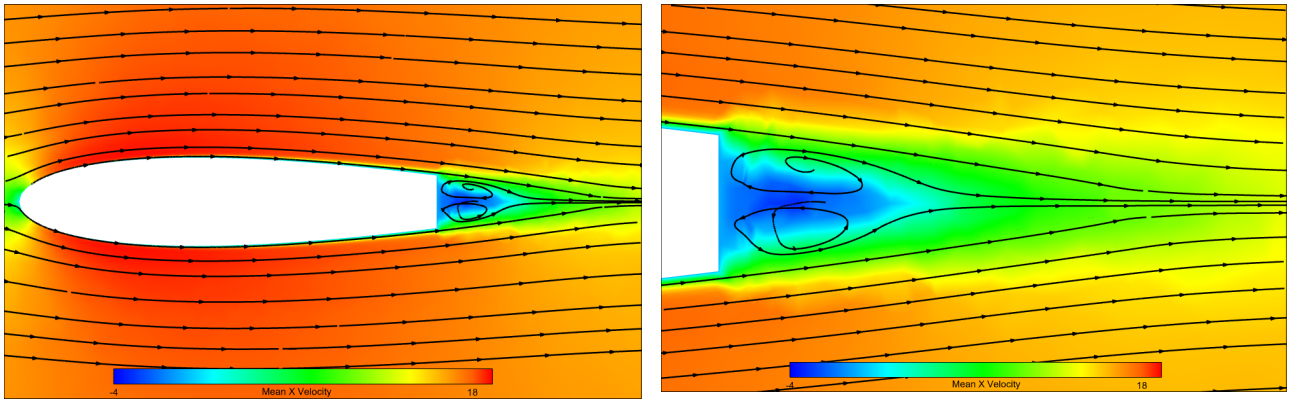

(c) Combed TE model (Root) (d) Close-up view at the root

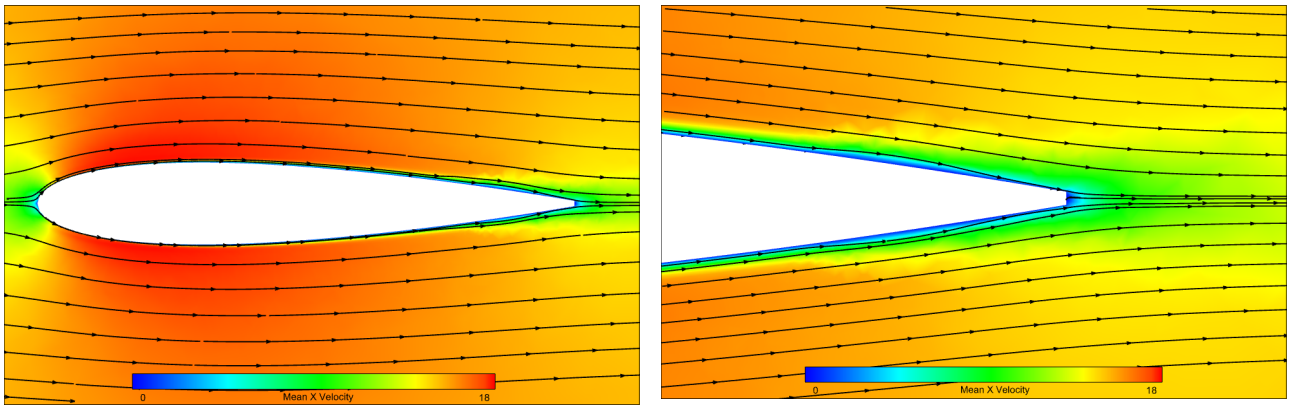

(e) Comb-Serrated TE model (Root) (f) Close-up view at the root

Fig. 12. X-velocity contour at the root of the modified models at $\alpha = 0^0$

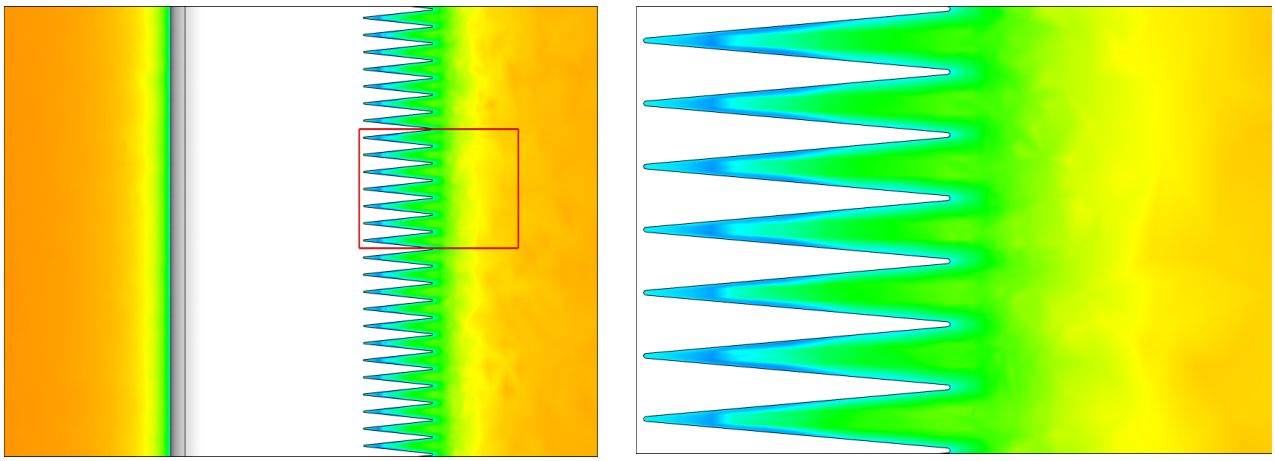

(a) Serrated TE model (Top View) (b) Close-up view of the TE

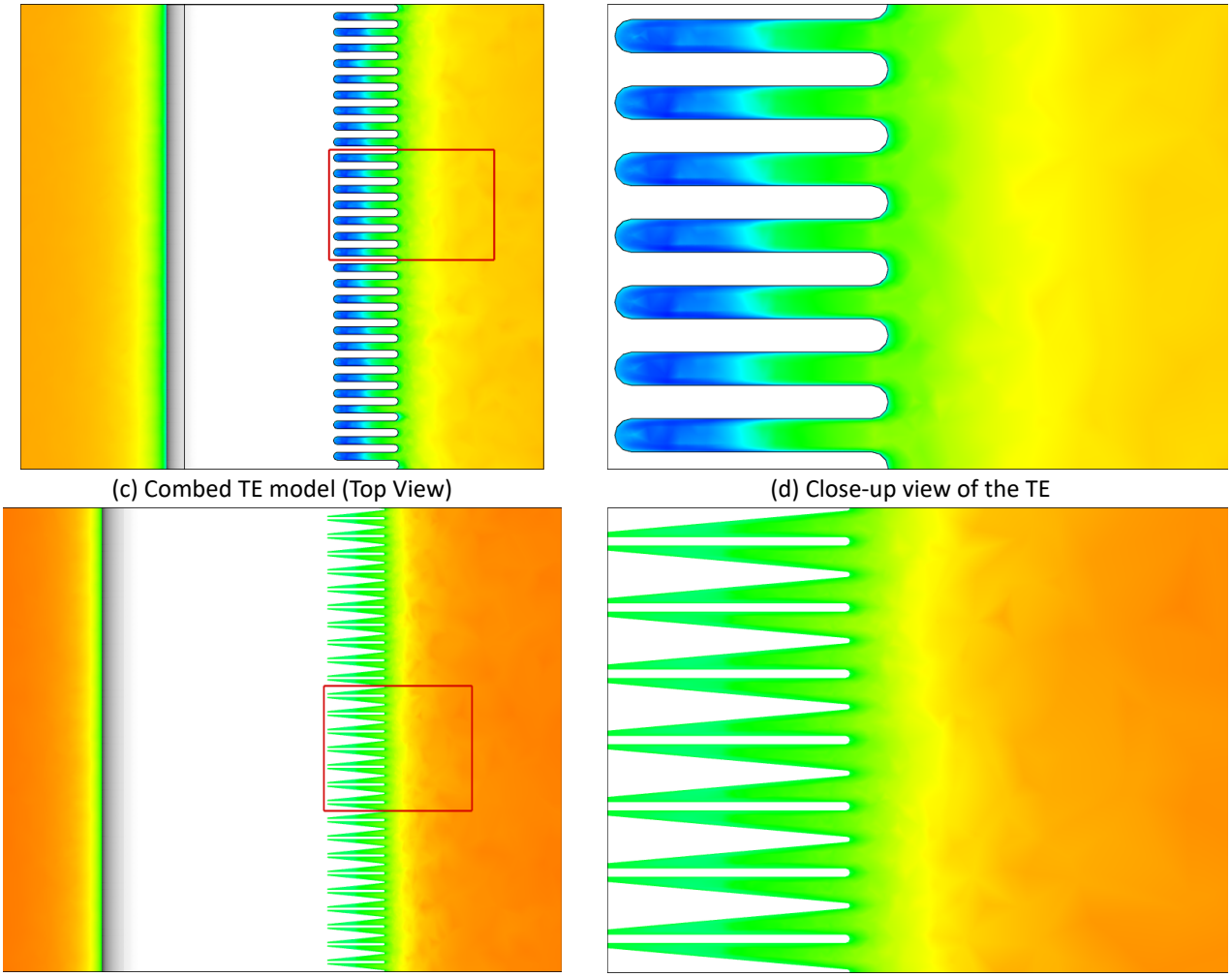

(c) Combed TE model (Top View) (d) Close-up view of the TE

(e) Comb-Serrated TE model (Top View) (f) Close-up view at the TE

Fig. 13. Top view contour of x-velocity component for the modified models at $\alpha = 0^0$

The velocity profile graph of serrated, comb, and comb-serrated configurations is provided in Figure 14 (a) to (b), Figure 15 (a) to (b) and Figure 16 (a) to (b). It offers a thorough illustration of the influence of modified trailing edges on the velocity distribution along the top surface of the airfoil. This graph demonstrates how the distinct property of each arrangement affects fluid flow. As represented in the velocity profile graph, the serrated trailing edge configuration shows an increase in fluid velocity away from the leading edge. At the tip and root of the trailing edge, the onset of separation and the development of vortices in the flow are noted at roughly 0.8c and 0.7c, respectively. This change leads to a drop in overall pressure levels on the serrated trailing edge, as illustrated clearly in Figure 14. On the other hand, the combed trailing-edge design does not demonstrate any separation along the tip, but a separation zone of roughly 0.7c is noted along the root of the trailing edge, as illustrated in Figures 11 and 12. As seen in the velocity profile graph, the comb-serrated model exhibits no separation zone along either the sawtooth-like or comb-like section. This flow characteristic is shown by a lack of sudden changes in the velocity gradient, which suggests continuous fluid flow along the surface of the airfoil.

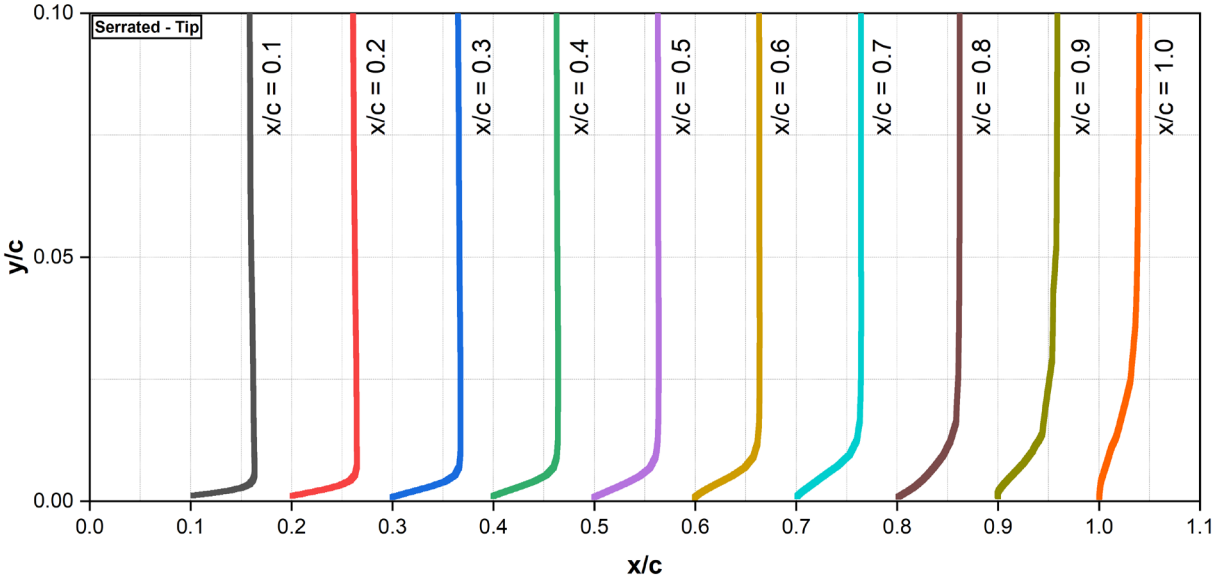

(a) Tip section of serrated trailing edge

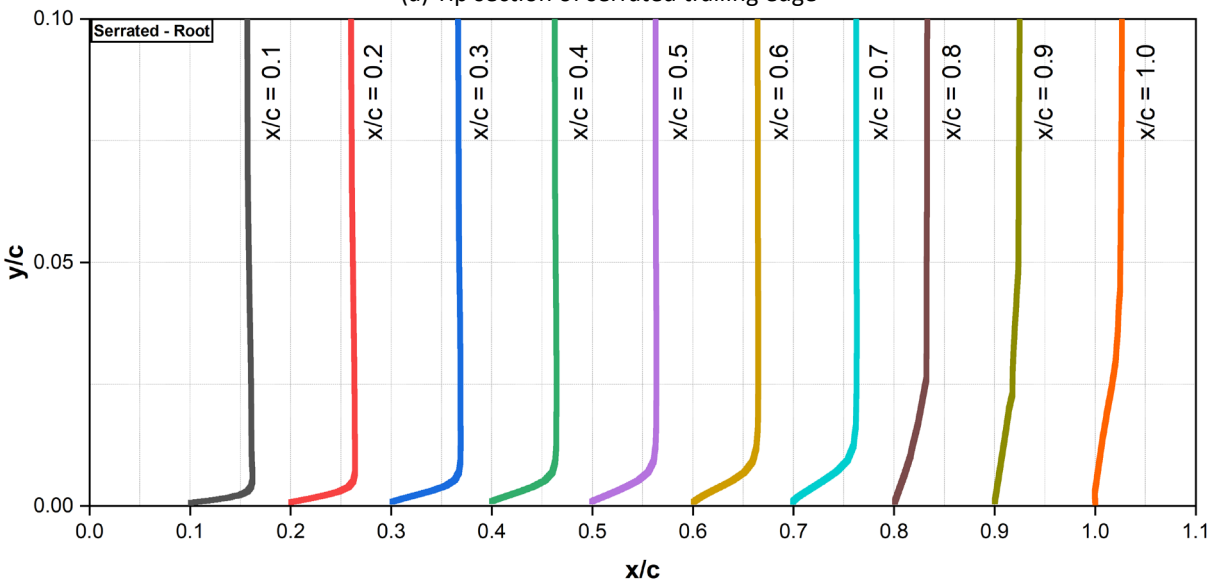

(b) Root section of serrated trailing edge

Fig. 14. Velocity profile of serrated TE configuration at $\alpha = 0^0$

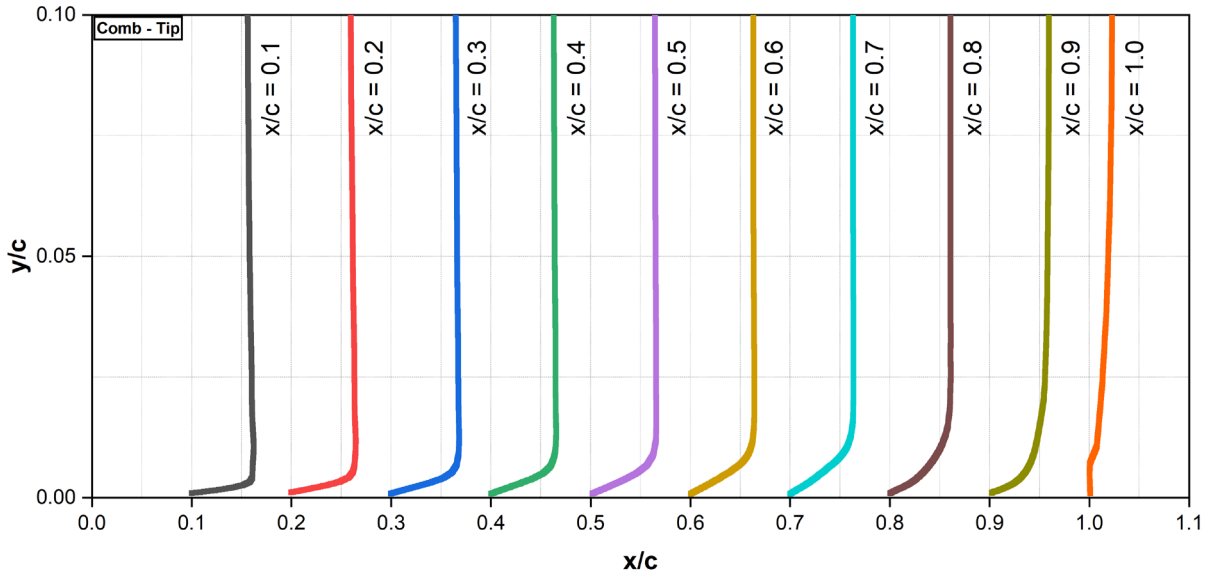

(a) Tip section of combed trailing edge

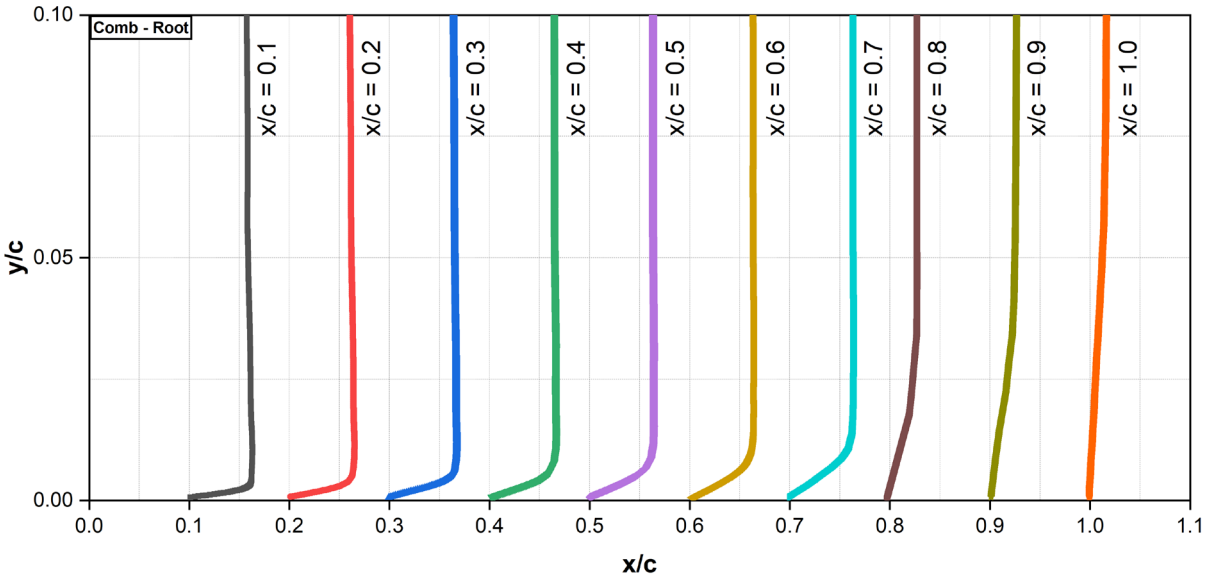

(b) Root section of combed trailing edge

Fig. 15. Velocity profile of combed TE configuration at $\alpha = 0^0$

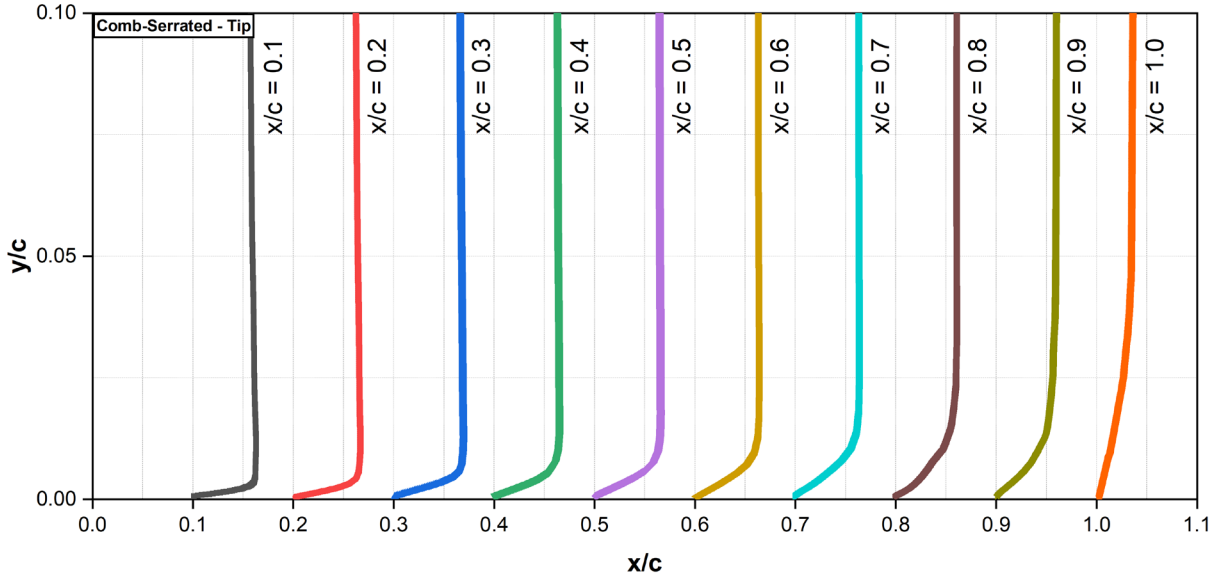

(a) Tip section of comb-serrated trailing edge

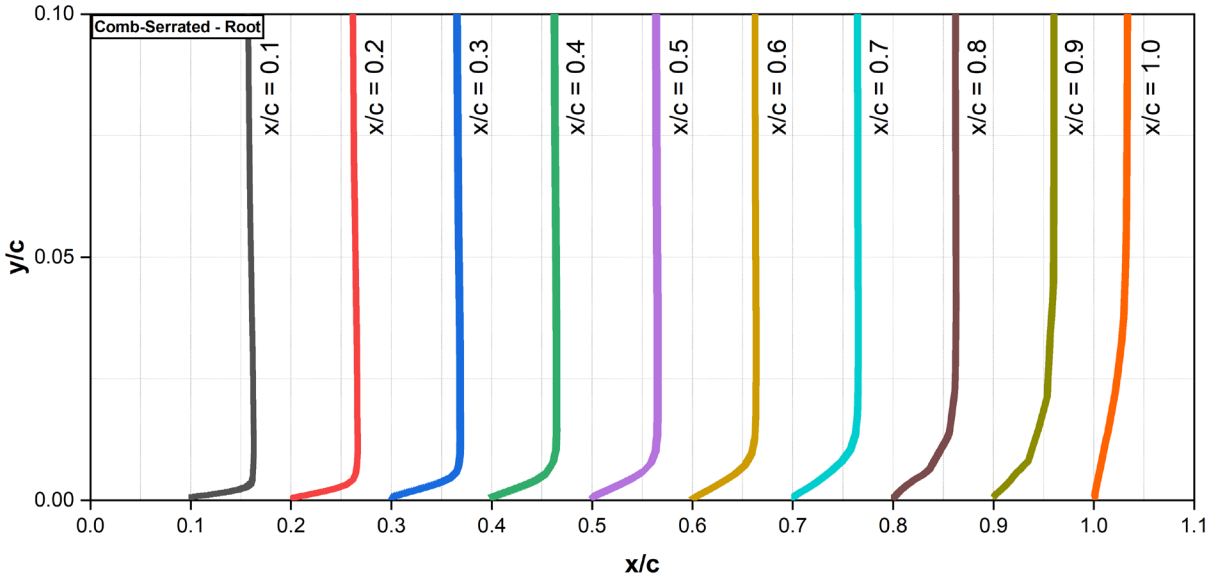

(b) Root section of comb-serrated trailing edge

Fig. 16. Velocity Profile of comb-serrated TE configuration at $\alpha = 0^0$

5. Conclusions

In conclusion, a detailed analysis of the results was undertaken numerically to understand the results fully. The numerical model was validated by its accuracy in capturing the aerodynamic features and flow structure, as proven by its prediction of lift fluctuations, mean lift coefficient, and flow structure. The pressure coefficient and skin friction coefficient graphs reveal that all modifications result in an early negative pressure zone and an uneven flow with greater skin friction values near the trailing edge relative to the baseline design. This flow pattern can be ascribed to the interaction between the flow and the redesigned trailing edges, which causes turbulence and boosts the fluid's momentum delivered to the airfoil's surface. The x-velocity contour analysis indicated that the serrated, combed, and comb-serrated models have more stable flow patterns and shorter separation bubbles when compared to the baseline configuration. Overall, the findings reveal that the serrated, combed, and comb-serrated airfoil designs each have a distinct impact on fluid flow.

The serrated trailing edge creates higher fluid velocity and pressure drop, while the combed trailing edge induces separation at the root and the comb-serrated design maintains a continuous fluid flow over the airfoil's surface.

Acknowledgement
The research was supported by the Ministry of Education (MOE) through the Fundamental Research Grant Scheme (FRGS/1/2018/TK09/UIAM/03/4). We would also like to thank IIUM for financial support under the KOE Postgraduate Tuition Fee Waiver Scheme 2019 (TFW2019).

References

[1] Ibren, Mohamed, Amelda Dianne Andan, Waqar Asrar, and Erwin Sulaeman. "A Review on Generation and Mitigation of Airfoil Self-Induced Noise." *Journal of Advanced Research in Fluid Mechanics and Thermal Sciences* 90, no. 1 (2022): 163-178. https://doi.org/10.37934/arfmts.90.1.163178..
[2] Carmichael, B. H. *Low Reynolds number airfoil survey, volume 1*. No. NASA-CR-165803-VOL-1. 1981.
[3] Alam, Muhammad, and Neil D. Sandham. "Direct numerical simulation of 'short' laminar separation bubbles with turbulent reattachment." *Journal of Fluid Mechanics* 410 (2000): 1-28. https://doi.org/10.1017/S0022112099008976
[4] Counsil, Joshua NN, and Kiari Goni Boulama. "Low-reynolds-number aerodynamic performances of the NACA 0012 and Selig-Donovan 7003 Airfoils." *Journal of aircraft* 50, no. 1 (2013): 204-216. https://doi.org/10.2514/1.C031856
[5] Malkiel, E., and R. E. Mayle. "Transition in a separation bubble." (1996): 752-759. https://doi.org/10.1115/1.2840931
[6] Ibren, Mohamed, Amelda Dianne Andan, Waqar Asrar, and Erwin Sulaeman. "Laminar Separation Bubble and Flow Topology of NACA 0015 at Low Reynolds Number." *CFD Letters* 13, no. 10 (2021): 36-51. https://doi.org/10.37934/cfdl.13.10.3651
[7] Crivellini, Andrea, Valerio D'Alessandro, Daniele Di Benedetto, Sergio Montelpare, and Renato Ricci. "Study of laminar separation bubble on low Reynolds number operating airfoils: RANS modelling by means of an high accuracy solver and experimental verification." In *Journal of Physics: Conference Series*, vol. 501, no. 1, p. 012024. IOP Publishing, 2014. https://doi.org/10.1088/1742-6596/501/1/012024
[8] Owen, P. R., and L. Klanfer. "On the laminar boundary layer separation from the leading edge of a thin aerofoil." (1955).
[9] Yuan, W., H. Xu, M. Khalid, and R. Radespiel. "A parametric study of LES on laminar-turbulent transitional flows past an airfoil." *International Journal of Computational Fluid Dynamics* 20, no. 1 (2006): 45-54. https://doi.org/10.1080/10618560600578492.
[10] Kurelek, John W., Burak A. Tuna, Serhiy Yarusevych, and Marios Kotsonis. "Three-Dimensional Development of Coherent Structures in a Two-Dimensional Laminar Separation Bubble." *AIAA Journal* 59, no. 2 (2021): 493-505. https://doi.org/10.2514/1.J059700.
[11] Lei, Juanmian, Feng Guo, and Can Huang. "Numerical study of separation on the trailing edge of a symmetrical airfoil at a low Reynolds number." *Chinese Journal of Aeronautics* 26, no. 4 (2013): 918-925. https://doi.org/10.1016/j.cja.2013.06.005
[12] Kim, Dong-Ha, and Jo-Won Chang. "Low-Reynolds-number effect on the aerodynamic characteristics of a pitching NACA0012 airfoil." *Aerospace Science and Technology* 32, no. 1 (2014): 162-168. https://doi.org/10.1016/j.ast.2013.08.018
[13] Plogmann, B., A. Herrig, and W. Würz. "Experimental investigations of a trailing edge noise feedback mechanism on a NACA 0012 airfoil." *Experiments in fluids* 54, no. 5 (2013): 1-14. https://doi.org/10.1007/s00348-013-1480-z
[14] Goni Boulama, Kiari, and Joshua Counsil. "Validation of a low-cost transitional turbulence model for low-Reynolds-number external aerodynamics." In *20th AIAA Computational Fluid Dynamics Conference*, p. 3698. 2011. https://doi.org/10.2514/6.2011-3698
[15] Ma, Dongli, Yanping Zhao, Yuhang Qiao, and Guanxiong Li. "Effects of relative thickness on aerodynamic characteristics of airfoil at a low Reynolds number." *Chinese Journal of Aeronautics* 28, no. 4 (2015): 1003-1015. https://doi.org/10.1016/j.cja.2015.05.012
[16] Jaafar, Reham K., M. A. Abdelrahman, Mina G. Mourad, Adnan A. Ateeq, and M. Moawed. "Modified Trailing Edge Impact on the Aerodynamic Performance of Wind Turbine Airfoil." *Journal of Advanced Research in Fluid Mechanics and Thermal Sciences* 91, no. 2 (2022): 133-144. https://doi.org/10.37934/arfmts.91.2.133144

[17] Chen, Nanshu, Hanru Liu, Qian Liu, Xingyu Zhao, and Yangang Wang. "Effects and mechanisms of LES and DDES method on airfoil self-noise prediction at low to moderate Reynolds numbers." *AIP Advances* 11, no. 2 (2021): 025232. https://doi.org/10.1063/5.0038183
[18] Selig, Michael, James Guglielmo, Andy Broern, and Philippe Giguere. "Experiments on airfoils at low Reynolds numbers." In *34th Aerospace Sciences Meeting and Exhibit,* p. 62. 1996. https://doi.org/10.2514/6.1996-62
[19] Lissaman, P. B. S. "Low-Reynolds-number airfoils." *Annual review of fluid mechanics* 15, no. 1 (1983): 223-239. https://doi.org/10.1146/annurev.fl.15.010183.001255
[20] Dassen, T., R. Parchen, J. Bruggeman, and F. Hagg. "Results of a wind tunnel study on the reduction of airfoil self-noise by the application of serrated blade trailing edges." (1996).
[21] Oerlemans, S., J. G. Schepers, G. Guidati, and S. Wagner. "Experimental demonstration of wind turbine noise reduction through optimized airfoil shape and trailing-edge serrations." (2001).
[22] Gruber, Mathieu, Phil Joseph, and Tze Pei Chong. "Experimental investigation of airfoil self noise and turbulent wake reduction by the use of trailing edge serrations." In *16th AIAA/CEAS aeroacoustics conference*, p. 3803. 2010. https://doi.org/10.2514/6.2010-3803
[23] Chong, Tze Pei, and Phillip F. Joseph. "An experimental study of airfoil instability tonal noise with trailing edge serrations." *Journal of Sound and Vibration* 332, no. 24 (2013): 6335-6358. https://doi.org/10.1016/j.jsv.2013.06.033
[24] Moreau, Danielle J., Laura A. Brooks, and Con J. Doolan. "Flat plate self-noise reduction at low-to-moderate Reynolds number with trailing edge serrations." In *Proceedings of ACOUSTICS*, pp. 2-4. 2011.
[25] Jones, Lloyd, and Richard Sandberg. "Numerical investigation of airfoil self-noise reduction by addition of trailing-edge serrations." In *16th AIAA/CEAS aeroacoustics conference*, p. 3703. 2010. https://doi.org/10.2514/6.2010-3703
[26] Sandberg, R. D., and L. E. Jones. "Direct numerical simulations of low Reynolds number flow over airfoils with trailing-edge serrations." *Journal of Sound and Vibration* 330, no. 16 (2011): 3818-3831. https://doi.org/10.1016/j.jsv.2011.02.005
[27] Chong, T. P., P. F. Joseph, and M. Gruber. "Airfoil self noise reduction by non-flat plate type trailing edge serrations." *Applied Acoustics* 74, no. 4 (2013): 607-613. https://doi.org/10.1016/j.apacoust.2012.11.003.
[28] Howe, Michael S. "Noise produced by a sawtooth trailing edge." *The Journal of the Acoustical society of America* 90, no. 1 (1991): 482-487. https://doi.org/10.1121/1.401273
[29] Lyu, Benshuai, Mahdi Azarpeyvand, and Samuel Sinayoko. "Prediction of noise from serrated trailing edges." *Journal of Fluid Mechanics* 793 (2016): 556-588. https://doi.org/10.1017/jfm.2016.132
[30] Chong, Tze Pei, and Alexandros Vathylakis. "On the aeroacoustic and flow structures developed on a flat plate with a serrated sawtooth trailing edge." *Journal of Sound and Vibration* 354 (2015): 65-90. https://doi.org/10.1016/j.jsv.2015.05.019
[31] Chong, Tze Pei, and Elisa Dubois. "Optimization of the poro-serrated trailing edges for airfoil broadband noise reduction." *The Journal of the Acoustical Society of America* 140, no. 2 (2016): 1361-1373. https://doi.org/10.1121/1.4961362
[32] Chaitanya, P., Phillip Joseph, Subramanyam Narayanan, and J. W. Kim. "Aerofoil broadband noise reductions through double-wavelength leading-edge serrations: A new control concept." *Journal of Fluid Mechanics* 855 (2018): 131-151. https://doi.org/10.1017/jfm.2018.620
[33] Lau, Alex SH, Sina Haeri, and Jae Wook Kim. "The effect of wavy leading edges on aerofoil-gust interaction noise." *Journal of Sound and Vibration* 332, no. 24 (2013): 6234-6253. https://doi.org/10.1016/j.jsv.2013.06.031
[34] Lyu, Benshuai, and Mahdi Azarpeyvand. "On the noise prediction for serrated leading edges." *Journal of Fluid Mechanics* 826 (2017): 205-234. https://doi.org/10.1017/jfm.2017.429
[35] Ra-mli, Muhammad Ridzwan, Wan Mazlina Wan Mohamed, Hamid Yusoff, Mohd Azmi Ismail, Ahmed Awaludeen Mansor, Azmi Hussin, and Aliff Farhan Mohd Yamin. "The Aerodynamic Characteristics Investigation on NACA 0012 Airfoil with Owl's Wing Serrations for Future Air Vehicle." *Journal of Advanced Research in Fluid Mechanics and Thermal Sciences* 102, no. 1 (2023): 171-183. https://doi.org/10.37934/arfmts.102.1.171183
[36] Vathylakis, Alexandros, Tze Pei Chong, and Phillip F. Joseph. "Poro-serrated trailing-edge devices for airfoil self-noise reduction." *AIAA journal* 53, no. 11 (2015): 3379-3394. https://doi.org/10.2514/1.J053983.
[37] Sueki, Takeshi, Takehisa Takaishi, Mitsuru Ikeda, and Norio Arai. "Application of porous material to reduce aerodynamic sound from bluff bodies." *Fluid dynamics research* 42, no. 1 (2010): 015004. https://doi.org/10.1088/0169-5983/42/1/015004
[38] Liu, Hanru, Jinjia Wei, and Zhiguo Qu. "Prediction of aerodynamic noise reduction by using open-cell metal foam." *Journal of Sound and Vibration* 331, no. 7 (2012): 1483-1497. https://doi.org/10.1016/j.jsv.2011.11.016

[39] Herr, Michaela, Karl-Stephane Rossignol, Jan Delfs, Nicolas Lippitz, and Michael Mößner. "Specification of porous materials for low-noise trailing-edge applications." In 20th AIAA/CEAS aeroacoustics conference, p. 3041. 2014. https://doi.org/10.2514/6.2014-3041
[40] Geyer, Thomas. "Trailing edge noise generation of porous airfoils." PhD diss., BTU Cottbus-Senftenberg, 2011.
[41] Lissaman, P. B. S. "Low-Reynolds-number airfoils." *Annual review of fluid mechanics* 15, no. 1 (1983): 223-239. https://doi.org/10.1146/annurev.fl.15.010183.001255
[42] Koh, Seong Ryong, Beckett Zhou, Matthias Meinke, Nicolas Gauger, and Wolfgang Schröder. "Numerical analysis of the impact of variable porosity on trailing-edge noise." *Computers & Fluids* 167 (2018): 66-81. https://doi.org/10.1016/j.compfluid.2018.02.015
[43] Carpio, Alejandro Rubio, Roberto Merino Martínez, Francesco Avallone, Daniele Ragni, Mirjam Snellen, and Sybrand van der Zwaag. "Experimental characterization of the turbulent boundary layer over a porous trailing edge for noise abatement." *Journal of Sound and Vibration* 443 (2019): 537-558. https://doi.org/10.1016/j.jsv.2018.12.010
[44] Bernicke, Paul, R. A. D. Akkermans, Varun B. Ananthan, Roland Ewert, Jürgen Dierke, and Lennart Rossian. "A zonal noise prediction method for trailing-edge noise with a porous model." *International Journal of Heat and Fluid Flow* 80 (2019): 108469. https://doi.org/10.1016/j.ijheatfluidflow.2019.108469
[45] Herr, Michaela, and Johann Reichenberger. "In search of airworthy trailing-edge noise reduction means." In *17th AIAA/CEAS Aeroacoustics Conference (32nd AIAA Aeroacoustics Conference)*, p. 2780. 2011. https://doi.org/10.2514/6.2011-2780
[46] Zhang, Minghui, and Tze Pei Chong. "Experimental investigation of the impact of porous parameters on trailing-edge noise." *Journal of Sound and Vibration* 489 (2020): 115694. https://doi.org/10.1016/j.jsv.2020.115694
[47] Revell, James, James Revell, Herbert Kuntz, Frank Balena, Clifton Horne, Bruce Storms, Robert Dougherty et al. "Trailing-edge flap noise reduction by porous acoustic treatment." In *3rd AIAA/CEAS aeroacoustics conference*, p. 1646. 1997. https://doi.org/10.2514/6.1997-1646
[48] Geyer, Thomas, Ennes Sarradj, and Christoph Fritzsche. "Porous airfoils: noise reduction and boundary layer effects." *International journal of aeroacoustics* 9, no. 6 (2010): 787-820. https://doi.org/10.1260/1475-472X.9.6.787
[49] Wang, Meng, and Parviz Moin. "Computation of trailing-edge flow and noise using large-eddy simulation." *AIAA journal* 38, no. 12 (2000): 2201-2209. https://doi.org/10.2514/2.895
[50] Wagner, Claus, Thomas Hüttl, and Pierre Sagaut, eds. Large-eddy simulation for acoustics. Vol. 20. Cambridge University Press, 2007. https://doi.org/10.1017/CBO9780511546143
[51] Oberai, Assad A., Farzam Roknaldin, and Thomas JR Hughes. "Computation of trailing-edge noise due to turbulent flow over an airfoil." *AIAA journal* 40, no. 11 (2002): 2206-2216. https://doi.org/10.2514/2.1582
[52] Storey, R. C., S. E. Norris, and J. E. Cater. "Modelling turbine loads during an extreme coherent gust using large eddy simulation." In *Journal of Physics: Conference Series*, vol. 524, no. 1, p. 012177. IOP Publishing, 2014. https://doi.org/10.1088/1742-6596/524/1/012177
[53] Kim, Sung-Eun. "Large eddy simulation using an unstructured mesh based finite-volume solver." In *34th AIAA fluid dynamics conference and exhibit*, p. 2548. 2004. https://doi.org/10.2514/6.2004-2548
[54] O magorinsky, Joseph. "General circulation experiments with the primitive equations: I. The basic experiment." *Monthly weather review* 91, no. 3 (1963): 99-164. https://doi.org/10.1175/1520-0493(1963)091<0099:GCEWTP>2.3.CO;2
[55] Germano, Massimo, Ugo Piomelli, Parviz Moin, and William H. Cabot. "A dynamic subgrid-scale eddy viscosity model." *Physics of Fluids A: Fluid Dynamics* 3, no. 7 (1991): 1760-1765. https://doi.org/10.1063/1.857955
[56] Zhao, Dan, Nuomin Han, Ernest Goh, John Cater, and Arne Reinecke. Wind turbines and aerodynamics energy harvesters. Academic Press, 2019
[57] Shen, Wen Zhong, Weijun Zhu, and Jens Nørkær Sørensen. "Aeroacoustic computations for turbulent airfoil flows." *AIAA journal* 47, no. 6 (2009): 1518-1527. https://doi.org/10.2514/1.40399
[58] Miley, Stan J. *Catalog of low-Reynolds-number airfoil data for wind-turbine applications.* No. RFP-3387. Rockwell International Corp., Golden, CO (USA). Rocky Flats Plant; Texas A and M Univ., College Station (USA). Dept. of Aerospace Engineering, 1982. https://doi.org/10.2172/5044823
[59] Jacobs, E., and Albert Sherman. "Airfoil section characteristics as affected by variations of the." *Report-National Advisory Committee for Aeronautics* 577-611 (1937): 227.